PHYSICAL REVIEW FLUIDS **4**, 053701 (2019)

Dynamics of nonlinear Alfvén waves in the shallow water magnetohydrodynamic equations

Martin Magill[*]
Faculty of Science, University of Ontario Institute of Technology, 2000 Simcoe St N, Oshawa, Ontario, Canada L1G 0C5

Aaron Coutino, Benjamin A. Storer, Marek Stastna, and Francis J. Poulin
Department of Applied Mathematics, University of Waterloo, 200 University Ave W, Waterloo, Ontario, Canada N2L 3G1

(Received 29 October 2018; published 1 May 2019)

The large-scale hydrodynamics of the solar tachocline have been modeled by a version of the well-known shallow water equations augmented to include the effects of magnetism. Due to the conservation of magnetic flux, these shallow water magnetohydrodynamic equations have an additional constraint that the classical shallow water equations (without magnetism) do not. This restricts the set of possible initial conditions, but in itself does not provide information about the dynamics. The linear theory of wave motion on both the f plane and β plane is relatively well documented. We thus seek to explore the dynamics of nonlinear waves on the magnetohydrodynamic f plane. By initializing with a circular vortex and no free surface displacement, we make contact with a substantial literature in geophysical fluid dynamics, satisfy the magnetohydrodynamic constraint, and provide a means to generate all possible wave species through the adjustment process. We find that for Cowling numbers typical of the solar tachocline, the response is dominated by zonally propagating Alfvén waves, which take the form of vortices. These vortices are expressed in the velocity, free surface, and magnetic field variables. We explore how nonlinearity and variation in the Cowling number affect these dynamical structures, finding that nonlinearity warps the axially symmetric Alfvén wave modes of linear theory. Moreover, while the waves maintain a fixed shape during pure propagation, we find that wave shape is significantly modified during collisions. The extent of warping during collisions is amplitude dependent, and hence a nonlinear effect, albeit one that is fundamentally different from soliton models of nonlinear waves in shallow water. We explore parameter ranges outside those relevant to our Sun's tachocline and find that our results are robust over significant portions of parameter space. In the limit of rapidly rotating stars (i.e., rates 100 times larger than those associated with our Sun) we find that the Alfvén waves destabilize over time.

DOI: 10.1103/PhysRevFluids.4.053701

I. INTRODUCTION

The shallow water (SW) equations are commonly used to model fluid mechanical problems with a free surface where the vertical length scale H is much smaller than the horizontal length scale L. The equations are derived by integrating the Euler equations over the vertical dimension, applying the boundary conditions at the surface and bottom, and assuming that the pressure in the fluid is hydrostatic. This is equivalent to a first-order perturbation expansion in the aspect ratio, or

---

[*] martin.magill1@uoit.net

$\epsilon = H/L$. In the case of large-scale motions of fluids on Earth and similar planets, often referred to as geophysical fluid dynamics (GFD), the SW equations have provided insight into both vortex and wave motions [1]. Extensions of classical SW theory have attempted to account for the dispersive behavior of short waves [2,3]. In this case, it is possible for nonlinearity and dispersion to balance so as to yield solitary waves: waves of permanent form that interact as solitons, i.e., in a particlelike manner [4].

A commonly considered example in SW theory is the so-called dambreak, or gravitational adjustment, problem in which a jump in the free surface height (or alternatively, layer thickness) is released from rest (i.e., water is suddenly released from behind a dam). In the nonrotating case, this is a classical problem in the theory of nonlinear hyperbolic partial differential equations, with a well-defined theory of shocks and rarefaction fans [4]. In the presence of rotation, however, even this simple problem (often labeled the geostrophic adjustment problem) has relatively recent contributions in the literature [5], with the extension to systems with short wave dispersion (such as continuously stratified fluids) under active discussion in the literature [6,7].

In the context of GFD, the traditional SW equations have proven to be very successful in process-oriented modeling of the large-scale behavior of oceans, large lakes, and aspects of atmospheric flow. Perhaps inspired by this, Gilman [8] proposed the SW magnetohydrodynamic (SMHD) equations. These are derived analogously to the SW equations, but now from the equations of magnetohydrodynamics, which are the Euler equations coupled to Maxwell's equations. Schecter *et al.* [9] conducted an analysis of the linear wave modes allowed for the SMHD equations in a rotating frame of reference and suggested that a necessary next step to understanding the SMHD equations will be reached when the evolution of an arbitrary initial condition can be understood in terms of classes of theoretically derived solutions. While this suggestion was made in the context of the solar tachocline, a problem for which the SMHD equations are well suited, various authors have conducted theoretical analyses of the equations in other mathematical and physical settings. De Sterck [10] conducted an analysis of the wave modes allowed by the one-dimensional SMHD equations, as well as the two-dimensional time-independent SMHD equations. Dellar [11] derived and analyzed a dispersive formulation of the equations. Gu *et al.* [12] analyzed global solutions to the one-dimensional equations. Shiue [13] discussed a one-dimensional boundary value problem formulation designed for the solar tachocline. Zeitlin [14] revisited the derivation of the rotating SMHD equations from a mathematical point of view, elucidating the underlying approximations and thereby the bounds of applicability of the equations. They extended their derivation to cover multilayer generalizations and studied the equations in the limit of strong rotation (which is a commonly explored limit in geophysical applications). Inevitably, however, all of these analyses reduce the dimensionality of the problem by at least one order, omitting either one of the spatial dimensions or evolution in time. The literature on the full two-dimensional equations is far more sparse. Zaqarashvili *et al.* [15] and Zaqarashvili *et al.* [16] derived dispersion equations for the linearized SMHD equations in Cartesian and spherical coordinates on the β plane and used these to study the dynamics of global magnetic Rossby waves. London [17] extended the asymptotic expansion behind the derivation of the SMHD equations and analyzed the resulting wave modes using the method of geometric optics, finding evidence for latitudinally trapped wave modes. Zeitlin *et al.* [18] explored a generalization of the geostrophic adjustment problem, which they called magneto-geostrophic adjustment. Using a 1.5-dimensional version of the SMHD equations, they successfully derived theoretical and numerical results. They also extended that derivation to the full two-dimensional SMHD equations and concluded that in both cases geostrophic adjustment resolves into two noninteracting flows: fast magneto-inertia-gravity waves and slow rotationally modified Alfvén waves.

Poulin *et al.* [19] compared numerical solutions of linear waves in SMHD theory for a spherical geometry with a latitudinally varying Coriolis force to a previously published analytical approximation [20]. They found that pseudospectral methods were always effective for computing the dispersion relation and the spatial structure of the various waveforms. The numerical calculations matched the approximate theory when rotation and the magnetic field were weak. However, the approximate theory was shown to break down for magnetic fields that are larger and rotation rates that are faster than those typical of our Sun. Thus even in the realm of linear theory, there are subtleties that preclude a tidy analytical presentation. Márquez-Artavia *et al.* [21] developed a relatively complete theory of SMHD linear waves and instabilities in a spherical geometry, concentrating on parameter regimes relevant to the Earth's core-mantle boundary. The authors suggest some observational ways to test their theory but caution against broadly applying their linear theory results to general stars and planets. Moreover, due to the the fact that these authors' focus is on equatorial situations, their results are not of direct relevance to the situation we model in this paper.

Numerical methods for the SMHD equations, along with the numerical analysis of these methods, have been presented by a number of authors. Kröger and Lukáčová-Medvid'ová [22] presented a finite volume Galerkin method. Qamar and Warnecke and Qamar and Mudasser [23,24] used several different methods: a version of the finite element method method in Ref. [23] and a kinetic flux-vector splitting method in Ref. [24]. Zia *et al.* [25] used a central-upwind finite difference method. However, these papers were primarily focused on analyzing the algorithms themselves, rather than using the numerical solvers as tools for conducting numerical experiments that probe the underlying dynamics.

In this work, we will primarily focus on the full, nonlinear SMHD equations in the context of the solar tachocline. The solar tachocline is an internal boundary layer occurring within the Sun and similar stars. It exists at the base of the outer convective layer, which is a turbulent and differentially rotating layer of plasma. Beneath the tachocline lies the radiative layer, in which a strong magnetic field forces the plasma to rotate with a constant angular velocity independent of latitude (except possibly at higher latitudes) [26]. The tachocline is remarkably thin, estimated at 4% of the solar radius [27], and is located roughly 70% of the solar radius from the center of the Sun [26]. The tachocline has been suspected to play an important role in solar dynamics since it was originally proposed by Spiegel and Zahn [28]. Dikpati *et al.* [27] recently proposed a detailed mechanism in which they suggest that solar weather originates in the tachocline. Wood and Brummell [29] published the first fully three-dimensional self-consistent numerical model demonstrating the emergence of a solar tachocline consistent with observations. Thus tachocline research is active and developing rapidly. At the same time, however, it is unclear what testable predictions simplified models like the SMHD equations yield.

In the context of GFD, vortex breakdown and instability is a classical problem with a substantial literature [30]. When rotation effects are important, breakdown can be induced when the vortex scale exceeds the preferred length scale of the system, which, in the GFD setting, is often the Rossby deformation radius. When the vortex scale sufficiently exceeds the deformation radius, instabilities serve to fracture the vortex into smaller vortices, the length scale of which is more commensurate with the deformation radius. For mildly unbalanced geophysical vortices, the adjustment process of reaching a balanced state radiates gravity waves into the system, leaving a balanced vortex after the adjustment resolves. Exploring the extent to which the above transfers to the setting of the solar tachocline is the primary goal of this paper.

We find that for Cowling numbers typical of the solar tachocline, vortex evolution is dominated by breakdown into zonally propagating Alfvén waves. These traveling vortices are expressed in the velocity, free surface, and magnetic field variables. We explore how nonlinearity and variation in the Cowling number affect these dynamical structures; we find that nonlinear effects warp the Alfvén wave modes, which otherwise exhibit axial symmetry in the linear regime of small perturbations. Moreover, while the waves maintain a fixed shape during pure propagation, we find that wave shape is significantly modified during collisions. The extent of warping during collisions is amplitude-dependent, and hence a nonlinear effect, albeit one that is fundamentally different from soliton models of nonlinear waves in shallow water. We explore parameter ranges outside those relevant to our Sun's tachocline and find that our results are robust over significant portions of parameter space. In the limit of rapidly rotating stars (i.e., for rotation rates 100 times larger than those that are associated with our Sun) we find that the Alfvén waves destabilize over time, with energy-containing structures located away from the latitudinal line of symmetry of the initial vortex.

Differential rotation plays an important role in the global dynamics of the solar tachocline [8,27]. Furthermore, one of the main applications of the SMHD model has been to study the instability of such differential rotation in the presence of a toroidal magnetic field. Nonetheless, in this work we omit differential rotation, instead following Schecter *et al.* [9], Zaqarashvili *et al.* [15], Zaqarashvili *et al.* [16], and Zeitlin *et al.* [18] in studying the dynamics local to a fixed latitude. Future work might explore how the vortex formation and propagation identified here are modified by differential rotation and other instabilities.

II. METHODS

A. Governing equations and dimensionless parameters

The equations of SMHD used for this work are those originally proposed by Gilman [8]:

$$h_t + \nabla \cdot (h\mathbf{u}) = 0, \tag{1}$$

$$\nabla \cdot (h\mathbf{B}_R) = 0, \tag{2}$$

$$u_t + \mathbf{u} \cdot \nabla u = -g_R \eta_x + fv + \mathbf{B}_R \cdot \nabla b_1, \tag{3}$$

$$v_t + \mathbf{u} \cdot \nabla v = -g_R \eta_y - fu + \mathbf{B}_R \cdot \nabla b_2, \tag{4}$$

$$(b_1)_t + \mathbf{u} \cdot \nabla b_1 = \mathbf{B}_R \cdot \nabla u, \tag{5}$$

$$(b_2)_t + \mathbf{u} \cdot \nabla b_2 = \mathbf{B}_R \cdot \nabla v. \tag{6}$$

Here $\mathbf{u}(x, y, t) = (u(x, y, t), v(x, y, t))$ is the velocity field, and $f = 2\Omega \sin \varphi$ is the Coriolis frequency, where Ω is the rate of rotation and φ is the latitude. Our model assumes a constant Ω throughout the simulation domain. It also assumes a flat topography, so that the total thickness of the fluid layer is $h(x, y, t) = H + \eta(x, y, t)$ where η is the perturbation of the free surface from its resting height. $g_R = g\frac{\rho_1 - \rho_2}{\rho_1}$ is the effective gravity, which is reduced by buoyancy. Here g is the actual gravitational acceleration and ρ_1, ρ_2 are the fluid densities above and below the free surface, respectively. The ratio $\alpha = \frac{\rho_1 - \rho_2}{\rho_1}$ is sometimes known as the Atwood number. There is considerable uncertainty in this value in the solar tachocline literature, as discussed below. $\mathbf{B}_R(x, y, t) = \frac{\mathbf{B}(x,y,t)}{\sqrt{\mu_0 \rho}}$ is the reduced magnetic field, where $\mathbf{B}$ is the physical magnetic field, μ_0 is the magnetic constant, and ρ is the (constant) density of the fluid. B_R has units of velocity. b_1 and b_2 are the components of the perturbation to the reduced magnetic field, hence added to the background reduced magnetic field. The background magnetic field was set to a strong toroidal field like the one hypothesized to permeate the tachocline, so that the reduced magnetic field is partitioned as

$$\mathbf{B}_R(x, y, t = 0) = \left(\frac{B_0}{\sqrt{\mu_0 \rho}}, 0\right) + (b_1(x, y, t), b_2(x, y, t)) \tag{7}$$

for all x, y. The nonzero component of the background reduced magnetic field is labeled as B_{R_0}. Table I lists the values assumed for the physical constants used in the baseline simulations. The baseline rotation rate Ω was set to that observed in the convective layer at a latitude of 65°. The estimate of the gravitational acceleration in the tachocline, g_{tach}, from the value at the Sun's surface, g_{surf}, neglects solar mass above the tachocline, but standard solar models (such as Ref. [31]) imply that the vast majority of the Sun's mass is located below the tachocline.

The dimensional groupings for the various terms in the equations and the corresponding physical mechanisms are given in Table II. We cannot independently choose all three of U, T, and L (the characteristic velocity, time, and length, respectively), so we adopt the advective timescale $T_A = L/U$, where the subscript A stands for "advection." Interestingly, the only way to create a length

TABLE I. Values of the physical constants used in the simulations. The subscript “surf” indicates values at the surface of the Sun, whereas “tach” indicates those in the tachocline.

Parameter	Value
$\Omega(\varphi)$ (degrees/day)	$A_\Omega + B_\Omega \sin(\varphi)^2 + C_\Omega \sin(\varphi)^4$[a]
A_Ω (degrees/day)	14.713[a]
B_Ω (degrees/day)	-2.396[a]
C_Ω (degrees/day)	-1.787[a]
φ	65°
$g = g_{\text{tach}}$ (m/s^2)	$g_{\text{surf}}(\frac{R_{\text{tach}}}{R_{\text{surf}}})^2 \approx 559$[b,c]
g_{surf} (m/s^2)	274[c]
R_{surf} (10^8 m)	6.955[c]
$R_{\text{tach}}/R_{\text{surf}}$	0.7[d]
H (10^6 m)	5[e]
ρ_{tach} (kg/m^3)	210[d]
α	0.01[e]
B_0 (T)	10[e]

[a] Reference [32].
[b] Reference [31].
[c] Reference [33].
[d] Reference [26].
[e] Reference [9].

scale based on a ratio of two different mechanisms is to take the ratio of the rotation terms with any other term in the equations. Furthermore, since B_{R_0} has dimensions of velocity, the magnetic mechanism does not correspond to a length scale unless it is balanced against other mechanisms. We will revisit this issue in the Results section. The dimensionless form of the momentum equations reads

$$u_t + \mathbf{u}\cdot\nabla u = -\frac{\eta_x}{\mathrm{Fr}^2} + \frac{v}{\mathrm{Ro}} + \mathrm{Co}^2(\mathbf{B}_R\cdot\nabla b_1), \tag{8}$$

$$v_t + \mathbf{u}\cdot\nabla v = -\frac{\eta_y}{\mathrm{Fr}^2} - \frac{u}{\mathrm{Ro}} + \mathrm{Co}^2(\mathbf{B}_R\cdot\nabla b_2), \tag{9}$$

where the three dimensionless numbers are the Rossby number, which measures the ratio of the inertia to the rotation term,

$$\mathrm{Ro} = \frac{U}{fL},$$

TABLE II. Terms in the SMHD equations.

Mechanism	Dimensional grouping
Acceleration	U/T
Inertia	U^2/L
Gravity	gH/L
Rotation	fU
Magnetism	$B_{R_0}^2/L$

TABLE III. Summary of simulation cases.

Case name	Description	Result
BASE	Baseline tachocline model	Vortex splitting into stable Alfvén waves
NO f	No rotation	Vortex splitting even without rotation
HIGH B_{R_0}	Doubled magnetic field	Doubled Alfvén wave speed
SMALLEST U_0	Small vortex amplitude	Circular Alfvén waves; linear collisions
NEGATIVE U_0	Reversed vortex polarity	Reflected Alfvén waves
LARGE U_0	Large vortex amplitude	Stretched Alfvén waves; nonlinear collisions
BSM	Small vortex width	No effect (no magnetic length scale)
LOW B_{R_0}	Decreased magnetic field	No vortex splitting; spiral; wave breaking
LOW B_{R_0} LOW U_0	Decreased both B_0 and U_0	Vortex splitting; winglike Alfvén waves
HIGH f	Increased rotation	Alfvén waves destabilize

the Froude number, which measures the ratio of the inertia to the gravity (or hydrostatic pressure) term,

$$\mathrm{Fr} = \frac{U}{\sqrt{g_R H}},$$

and the Cowling number, which measures the ratio of the magnetic and inertial terms,

$$\mathrm{Co} = \frac{B_{R_0}}{U}.$$

The parameters U and L are given by representative values of the initial conditions for our simulations, the initial radius of the vortex and the maximum vortex-induced velocity. Note that the Cowling number is a ratio of velocities, in analogy with the inverse Froude number, but for reasons of consistency with the literature the Cowling number has the wave speed in the numerator and the speed associated with the dynamics in the denominator. Hence it is the reciprocal of the Cowling number that is the magnetic analog of the Froude number. For the simulations discussed below (see Table III for an outline of the various cases), the dimensionless parameters are given in Table IV. We note that the ratio of the magnetic Rossby number Ro_m and the Rossby number Ro in Zeitlin *et al.* [18] gives the Cowling number.

Besides the advective timescale $T_A = L/U$ given above, other timescales can be derived from the SMHD equations. For instance, demanding that the acceleration and magnetism terms balance

TABLE IV. Dimensionless numbers by simulation case.

Case name	Ro	Fr	Co	1/Co	T_M (s)	T_A (s)
BASE	3.7	0.07	1.23	0.812	4.5×10^4	6.8×10^4
NO f	∞	0.07	1.23	0.812	4.5×10^4	6.8×10^4
HIGH B_{R_0}	3.7	0.07	2.46	0.41	1.1×10^4	6.8×10^4
SMALLEST U_0	0.37	0.0067	12.3	0.081	4.5×10^3	6.8×10^5
NEGATIVE U_0	3.7	0.07	1.23	0.812	4.5×10^4	6.8×10^4
LARGE U_0	7.35	0.134	0.62	1.62	9.0×10^4	3.4×10^4
BSM	7.35	0.07	1.23	0.812	2.2×10^4	3.4×10^4
LOW B_{R_0}	3.7	0.07	0.123	8.12	4.5×10^6	6.8×10^4
LOW B_{R_0} LOW U_0	1.84	0.03	0.246	4.061	2.24×10^6	1.4×10^5
HIGH f	0.037	0.07	1.23	0.812	4.5×10^4	6.8×10^4

produces a magnetism-based (hence the subscript M) timescale,

$$T_M = \frac{UL}{B_{R_0}^2}.$$

In Sec. III the results of the simulations are presented based on this timescale T_M, since it proved useful for characterizing separation of leftward and rightward propagating waves from the initial condition. Timescales based purely on rotation $T_R = 1/f$ and buoyancy $T_B = \sqrt{g/H}$ may be defined, but for the parameter regime explored in our work the magnetism-based timescale, T_M, proved far more useful.

Finally, following standard arguments from geophysical fluid dynamics (e.g., Ref. [1]) we define the Rossby deformation radius as

$$L_D = \frac{\sqrt{g_R H}}{f}.$$

B. The vortex adjustment problem

Since the governing SMHD equations were obtained as an extension of the geophysical SW equations, it is natural to try the initial conditions used in geostrophic adjustment problems, such as a perturbation in the surface height of an initially stationary fluid. However, in the presence of a predominantly toroidal field such as the one in the solar tachocline, perturbing the free surface without perturbing the magnetic field violates the conservation of magnetic flux in the z direction of the SMHD equations. Such a violation corresponds to an imperfectly conducting plasma, but the SMHD equations do not include the additional ohmic resistive terms required to correctly represent such a plasma. Thus the initial conditions of geostrophic adjustment are not directly compatible with the physical model represented by this simple SMHD model. Zeitlin *et al.* [18] extended the dambreak problem by perturbing the magnetic field to conserve flux.

Here, instead, we will study the vortex adjustment problem, in which we start with a uniform layer thickness and a purely toroidal magnetic field. The perturbation is introduced as a vortex in the velocity field. The solver used for this work preserves the magnetic flux specified in the initial conditions. Thus if the magnetic flux is zero initially, this property will be preserved (this was noted previously by Mak *et al.* [34]).

The velocity field was initialized as a modified Gaussian vortex, analogous to a Rankine vortex in classical vortex dynamics [35]. It is given by

$$u(x, y, t = 0) = +2U_0 \frac{y}{L_0} \exp\left[-\frac{(x^2 + y^2)}{L_0^2}\right], \tag{10}$$

$$v(x, y, t = 0) = -2U_0 \frac{x}{L_0} \exp\left[-\frac{(x^2 + y^2)}{L_0^2}\right], \tag{11}$$

where U_0 and L_0 are prescribed initial velocity and length scales. A vortex was chosen because its circular symmetry allows us to ascertain to what extent wave propagation leads to latitudinal trapping. While the Gaussian profile is only one of many possible choices of radial structure, explorations with other functional forms have shown that the dominant dynamical features of the vortex evolution are not very sensitive to the precise structure of the initial vortex but are instead set by the bulk parameters of the problem.

Since the magnetic field is dominated by the strong, toroidal background state, it is important to define a measure of the perturbation magnetic field. We choose to employ the perturbation magnetic field energy (PMFE) for this purpose. The PMFE is motivated by expanding the magnetic energy density in terms of the background field $(B_{R_0}, 0)$ and the perturbation on that field, (b_1, b_2), to obtain

$$E_{\mathrm{mag}} = \frac{1}{2\mu}\mathbf{B}_R^2 = \frac{1}{2\mu}\left[\left(B_{R_0} + b_1\right)^2 + b_2^2\right]$$
$$= \frac{1}{2\mu}\left[B_{R_0}^2 + 2B_{R_0}b_1 + \left(b_1^2 + b_2^2\right)\right].$$

From this, the PMFE is defined to be

$$\mathrm{PMFE} := \frac{1}{2\mu}\left(b_1^2 + b_2^2\right) = \frac{1}{2\mu}\left(\mathbf{B} - \mathbf{B}_{R_0}\right)^2.$$

The total magnetic field energy is therefore the sum of the background magnetic field energy, which is constant and thus cannot contribute to system dynamics, the PMFE, and a mixed term indicating the energy of interaction between the background magnetic field and the perturbation in the field. We found the PMFE to be a useful indicator of the structure of the magnetic field deformation. In particular, the PMFE is non-negative, making it appropriate for comparison to other common scalar metrics based on the velocity field like enstrophy (one half of the vorticity squared), kinetic energy, and available potential energy (proportional to the free surface height squared) [1].

C. Numerical methods and simulation parameters

The code used for the simulations was designed and tested in Matlab, with the production version subsequently written in C using OpenMP for parallelization. The code builds on previous solvers for the weakly nonhydrostatic SW equations [36] and solves the SMHD equations with doubly periodic boundary conditions using FFT-based pseudospectral methods in space and a leap-frog time-stepping scheme for each variable of interest. Aliasing due to the nonlinear terms was controlled by the application of an exponential spatial filter [37]. Extensive testing suggests the precise form of the filter does not affect the form of the solution. Grid halving and doubling tests were carried out to ensure all reported results are grid independent, and a suite of tests using small-amplitude initial conditions based on linear theory was used to ensure correct propagation speeds for the various wave types in the model. The C code was also validated against the Matlab prototype to ensure identical results. The code is available from the authors upon request.

The model domain is taken to be larger than a formal, local f-plane approximation (10° in latitude, or in the meridional direction, and 25° in longitude, or in the zonal direction). Mathematically, this choice of a large domain is sensible because we wish to allow the dynamics to evolve as long as possible before propagating waves interact across the periodic boundaries. In the meridional direction, this turns out to be an unnecessary precaution, due to the strong latitudinal trapping observed (and previously predicted theoretically [17]). We nevertheless maintain the large domain, since the code is efficient and allows for fast computation even for large grids. This allows us to extract subdomains focusing on regions of interest, while maintaining confidence that isolated events are indeed isolated. The large size of the domain implies that meaningful dimensionless parameters should be defined on the basis of dynamical features in the simulations (e.g., initial conditions) as opposed to the domain size.

We have selected the baseline parameters of our numerical model according to the published estimates of the physical conditions in the solar tachocline, listed in Table I. As we are interested in phenomena where magnetic effects are nontrivial, we start with a magnetic field intensity of 10 T. This is consistent with the range of peak magnetic forces estimated experimentally and used in other numerical experiments [9,26,27]. The standard solar model of Christensen-Dalsgaard [38], referred to by Schecter *et al.* [9], can be used to derive a range of α values, with values from 10^{-6} up to 10^{-4} appropriate for the overshoot layer of the tachocline, and much larger values of 0.01 to 0.3 appropriate for the radiative layer of the tachocline. The results in Sec. III fix $\alpha = 0.01$ and hence focus on the radiative layer. The majority of our experiments vary the physical constants f and B_{R_0}

and the vortex parameter U_0 and L_0. However, results exploring variations of α will be mentioned in Sec. IV. The remaining physical parameters used in this model are fixed to those in Table I.

III. RESULTS

We carried out a large number of numerical experiments and present a subset of these with the goal of answering the following questions:

(1) How does an initially circularly symmetric vortex evolve on the SMHD f plane?

(2) In what manner is nonlinearity manifested in this evolution, especially with respect to Alfvén waves?

(3) Is the shape of the propagating Alfvén waves always that of the initial vortex?

(4) How robust is the behavior observed for parameters based on the solar tachocline?

These four questions will be discussed in sequential order. In terms of the relevant figures for the questions posed above, question 1 is explored in Figs. 1 and 2, question 2 is explored in Figs. 3 to 7, question 3 is explored in Figs. 8 to 10, and question 4 is explored in Figs. 8 to 13. Note that there is some overlap between the discussion of questions 3 and 4. Since question 4 involves the exploration of a large parameter space, we focus on three detailed sets of numerical experiments: By reducing the strength of the magnetic field we were able to simulate the dynamics of spirallike states which did eventually lead to breaking. By reducing the strength of the initial vortex we were able to generate propagating Alfvén waves that bore no resemblance to the initial vortex. Alternatively, by increasing the rate of rotation by a factor of 100 we were able to destabilize the propagating Alfvén waves.

The governing SMHD equations do not have a means to dissipate energy, hence states that form shocks need careful interpretation. However, for the majority of parameter space explored it proved difficult to induce wave breaking and shock formation. For the purpose of the figures, the kinetic energy and PMFE are scaled based on the initial velocity and B_{R_0}, respectively, and plots are saturated at 0.25. The x and y coordinates are shown as fractions of the horizontal extent of the domain (i.e., the largest length scale in the simulation).

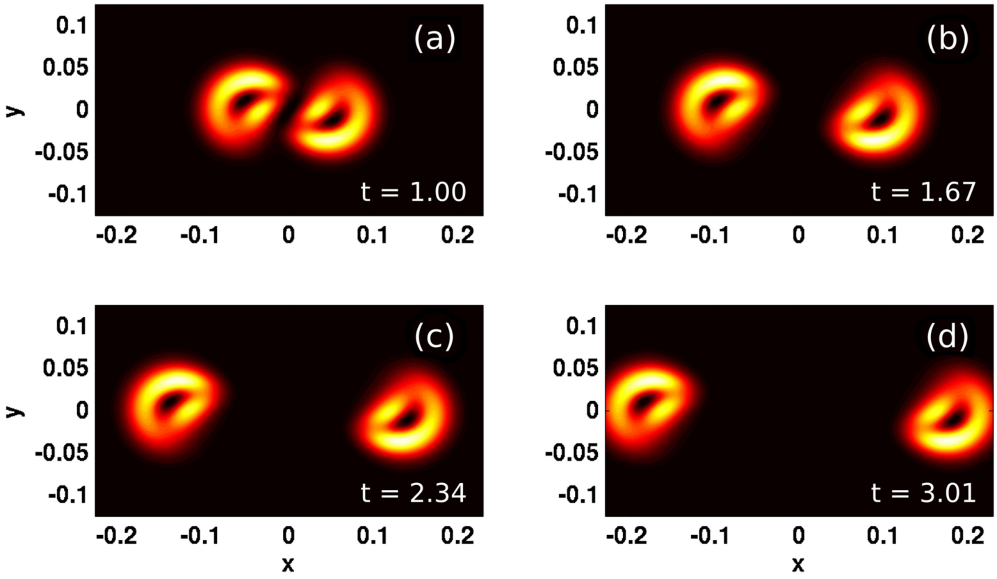

FIG. 1. Evolution of the kinetic energy in the baseline case (BASE). Panels (a)–(d) show times $t = 1.0, 1.67, 2.34, 3.01$, respectively.

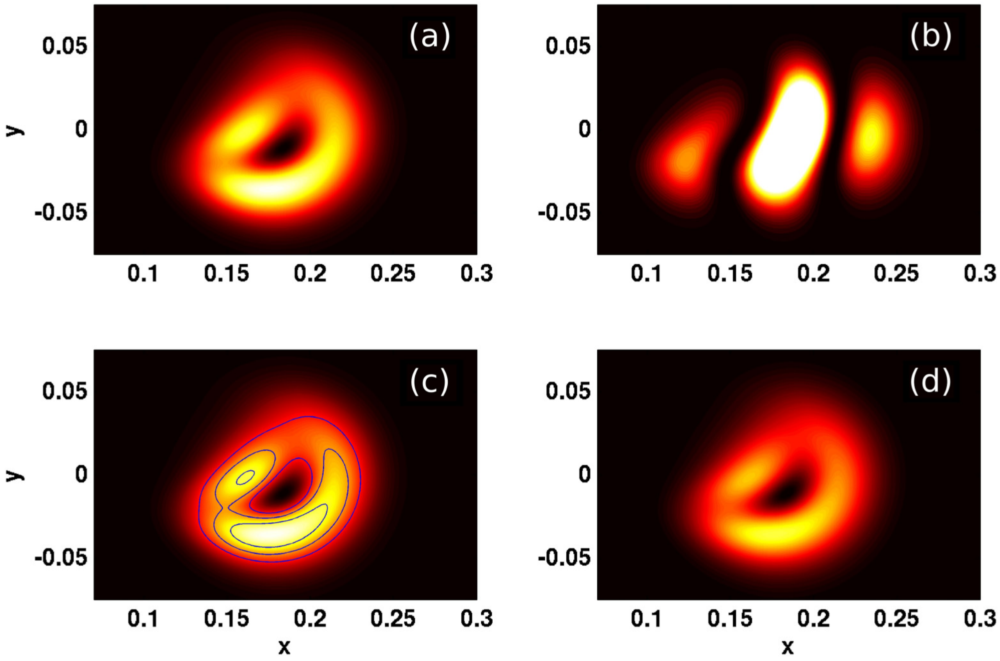

FIG. 2. Plots of (a) the kinetic energy, (b) the enstrophy, and (d) the PMFE in the baseline case (BASE). (c) The kinetic energy with isolines of the PMFE overlain. The time shown, $t = 3.01$, corresponds to Fig. 1(d).

A. Parameter regime for the Sun's tachocline

In Fig. 1 we show the evolution of the kinetic energy for the case labeled as BASE. Recall that the dimensionless parameters have velocity and length scales based on the initial vortex. For the BASE case the length scale is 3.4 times the assumed tachocline thickness or roughly 3.4×10^7 m. Alternatively, this means the aspect ratio set by the ratio of the layer depth H to the vortex length

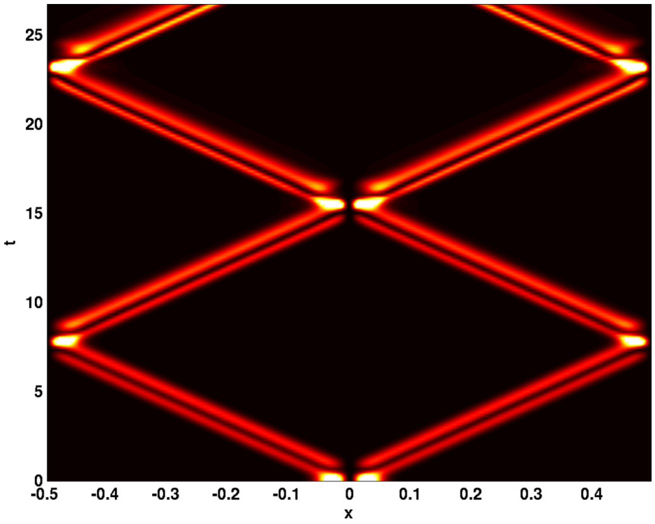

FIG. 3. Space-time plot of the kinetic energy profile along the $y = 0$ transect showing that during collisions wave shape is altered, but during propagation between collisions the wave shape remains unchanged.

scale L is 0.3. The ratio of the vortex length scale L to the Rossby radius L_D is 0.02, hence rotation effects are expected to be weak. From Fig. 1, it can be seen that the initially radially symmetric vortex separates into two donutlike propagating structures that propagate zonally. The rightward- and leftward-propagating features, while not radially symmetric, are reflections of one another provided one reflects across both $y = 0$ and $x = 0$. Figure 2 shows the three scalar fields of motion, the kinetic energy [Figs. 2(a) and 2(c)], the enstrophy [Fig. 2(b)], and the PMFE [Figs. 2(c) and 2(d)]. The time shown corresponds to Fig. 1(d). The initial radial symmetry of the enstrophy field can be seen to be fundamentally altered, with a prominent zonal banding structure. The PMFE field follows essentially the same geometrical distribution as the KE field; this is highlighted in Fig. 2(c), in which contours of PMFE are overlaid on the KE field. This implies that the perturbations to the magnetic field and the kinetic energy are "locked" together. The primary perturbation to the magnetic field is evidently due to the dragging of magnetic field lines by the flowing fluid. While these features are reminiscent of geostrophic balance in GFD, we have carried out a numerical experiment with $f = 0$, the case NO f (not shown), and found that the dynamics are essentially unchanged. This suggests that the dynamics in the solar tachocline are controlled by a far different balance than those in GFD theories of planetary atmospheres and oceans.

For early times the donutlike structures appear to propagate without changing form. Below we will show that the shape of these finite-amplitude Alfvén waves depends nonlinearly on U_0. First, however, we demonstrate that they are modified by head-on collisions with other waves. Figure 3 shows a space-time, or Hovmöller, plot for the kinetic energy along the $y = 0$ transect during multiple collisions in the BASE case. It is evident that the propagation speed remains essentially constant over the entire simulation. Due to the periodic boundary conditions the collisions occur between the rightward- and leftward-propagating waves when they reach the boundary and then again later in the middle of the domain. Moreover, while the wave shapes are clearly modified during the collisions, the waves appear to continue propagating without deformation between collisions. By fitting a line to the space-time plot (not shown in figures) it is possible to confirm that no phase shift is associated with the collisions, as would be the case for soliton interactions. Despite the seemingly linear behavior of the collisions, the waveforms are fundamentally altered during each collision. This is demonstrated in Fig. 4, which shows the kinetic energy before the first collision and after one, two, and three head-on collisions. Each collision profoundly modifies the donutlike shape, amplifying the asymmetry across $y = 0$. The shape does not continue to change after a collision, but rather remains essentially unchanged until the next collision. Detailed calculations shifting to a moving frame of reference suggest that fluctuations of the wave shape never manifest as more than 1% of the maximum kinetic energy. Taken together, these result suggest that nonlinearity is important during collisions, but the donutlike structures observed are not solitonlike in nature.

The estimated donut propagation speed ($608\,\mathrm{m\,s^{-1}}$ in dimensional form) matches B_{R_0} nearly exactly. In the HIGH B_{R_0} case (not shown in the figures) the propagation speed is $1272\,\mathrm{m\,s^{-1}}$, which again essentially matches B_{R_0}. There is essentially no difference in propagation speed from the BASE case to the SMALLEST U_0 case, though a comparison of zonal slices along $y = 0$ demonstrates that the structure in the BASE case is a bit more compact. Since B_{R_0} is the Alfvén wave velocity, these results suggest that the response to the vortex adjustment problem in parameter regimes relevant to the Sun's tachocline consists of finite-amplitude Alfvén waves.

In Fig. 5 we show the kinetic energy for the cases labeled as BASE and NEGATIVE U_0 at the same time as Fig. 1(d). The reversal of polarity of the initial vortex leads to a reflection of the kinetic energy distribution across $y = 0$. No other differences are evident, in the sense that the response is again a pair of finite-amplitude Alfvén waves propagating without changing shape.

The shape of these waves is modified from the radially symmetric initial state by finite-amplitude effects. This is demonstrated in Fig. 6, where we show the kinetic energy for the cases labeled as SMALLEST U_0, BASE, and LARGE U_0 in increasing order of U_0 from left to right. The kinetic energy in the top row of images [Figs. 6(a)–6(c)] is shown at the same time as Fig. 1(d). Only the rightward-propagating structures in the right half of the computational domain are shown. It is clear that the tenfold reduction in amplitude of the initial vortex decreases the breaking of radial

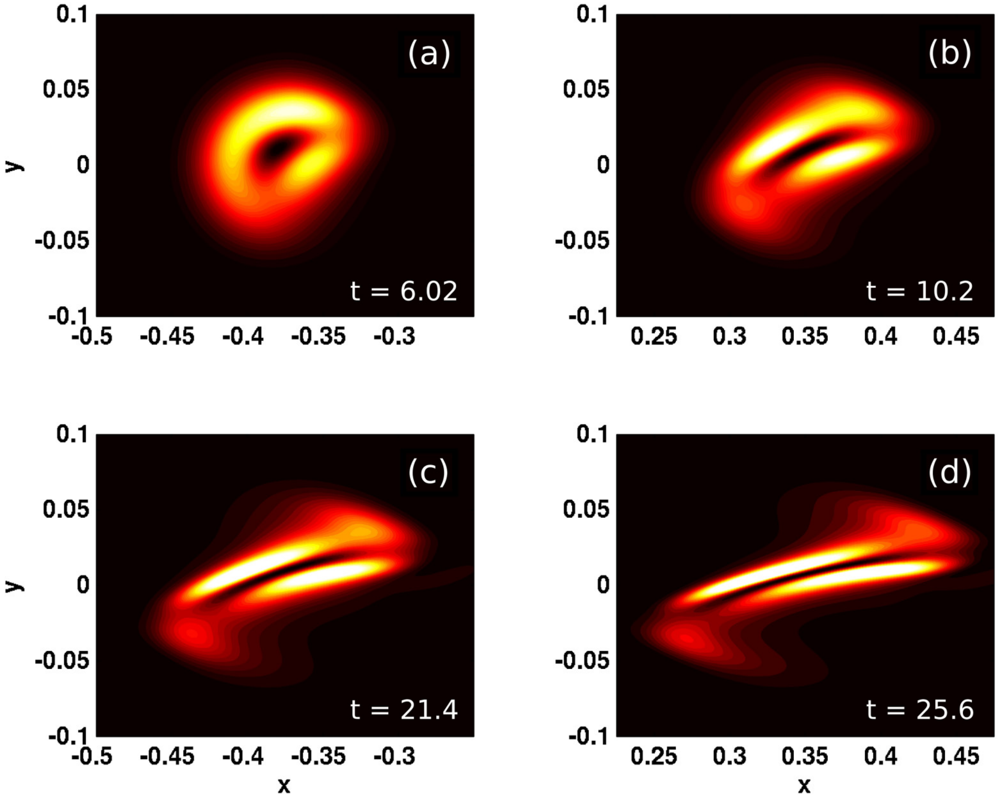

FIG. 4. Comparison of the kinetic energy in the baseline case (BASE) (a) before and after (b) one, (c) two, and (d) three head-on collisions. Panels (a)–(d) show times $t = 6.02, 10.2, 21.4, 25.6$, respectively.

symmetry to the point where the propagating structure appears to be essentially radially symmetric. In the case with larger initial velocities [Fig. 6(c)] the nonlinear effects are accentuated to the point that the radially symmetric vortex witnessed at lower velocities is warped to resemble a crescent moon shape. Despite these changes in shape, the propagation speed is unchanged from the values reported above, i.e., B_{R_0}.

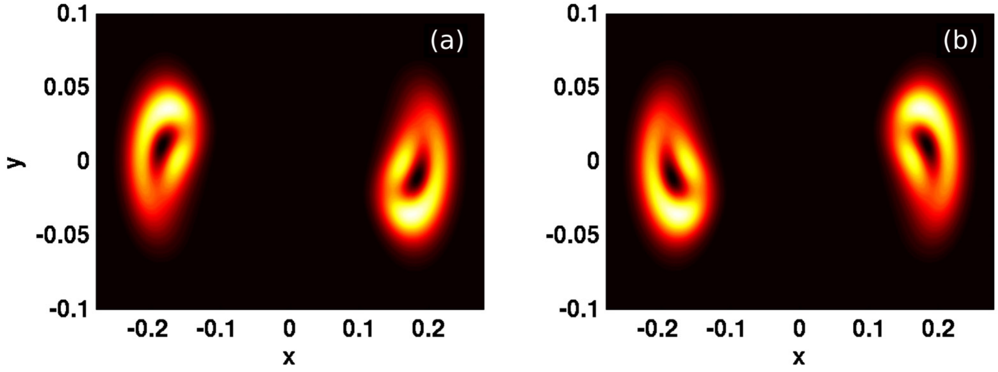

FIG. 5. Comparison of the kinetic energy distributions in the propagating waveforms (a) in the baseline (BASE) case and (b) when the polarity of the initial vortex is reversed (NEGATIVE U_0) at $t = 3.01$.

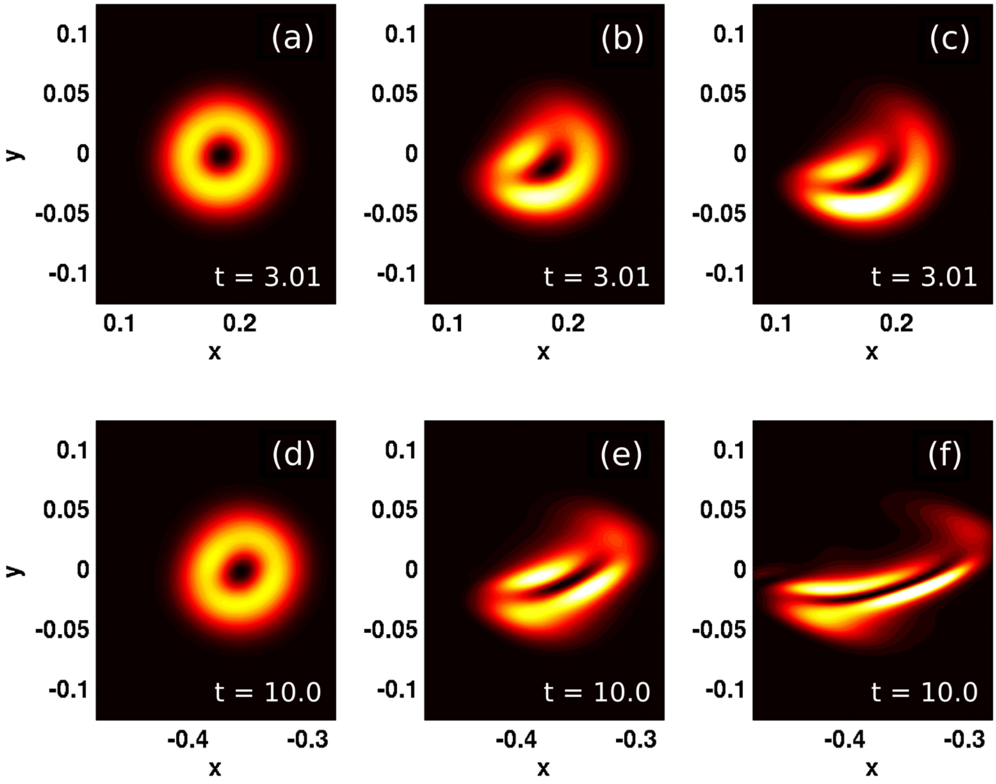

FIG. 6. Comparison of the kinetic energy distributions in the propagating waveform (a)–(c) before and (d)–(f) after collision as amplitude changes. Initial velocity reduced by a factor of 10 (case SMALLEST U_0) shown on left (a), (d); the baseline (BASE) case shown in the middle (b), (e); and the initial velocity doubled case (LARGE U_0) shown on the right (c), (f). Note the nearly perfect circular symmetry in the SMALLEST U_0 case, in panel (a), which is only slightly disturbed after the collision, in panel (d). The top row (a)–(c) shows rightward propagating waveforms before a collision ($t = 3.01$), while the bottom (d)–(f) shows the waveform after one collision ($t = 10$).

In the bottom row [Figs. 6(d)–6(f)] we show the shape of the waves after one collision. It can be seen that in Fig. 6(d), the case that is closest to “linear waves,” the radial symmetry is very nearly maintained, though even here some azimuthal variability is visible after the collision. As the amplitude is increased, the collision leads to a greater modification of the waveform, with the largest amplitude case leading to a stretching in the zonal direction and stronger banding in the meridional direction [Fig. 6(f)]. For all cases shown, the Froude number remains small (i.e., considerably less than 0.2).

As pointed out in Sec. II, the magnetic field terms do not have an associated inherent length scale. Since the propagating structures shown in Figs. 1 and 2 appear to be locked to the magnetic field, a change of length scale of the initial vortex should leave them essentially unchanged. In Fig. 7 we show the kinetic energy for the cases labeled as BASE and BSM at the same time as Fig. 1(d). Only a subdomain near the rightward-propagating structure is shown. Figure 7(c) is shown with the length scales halved. Visual inspection suggests that, as predicted, the structure, though clearly deformed from radial symmetry by finite-amplitude effects, is essentially unchanged by the change of length scale. Some minor differences are visible near the leading edge. The BSM case has a ratio of the vortex length scale L to the Rossby radius L_D of 0.01, hence rotation effects are expected to be even weaker than in the BASE case.

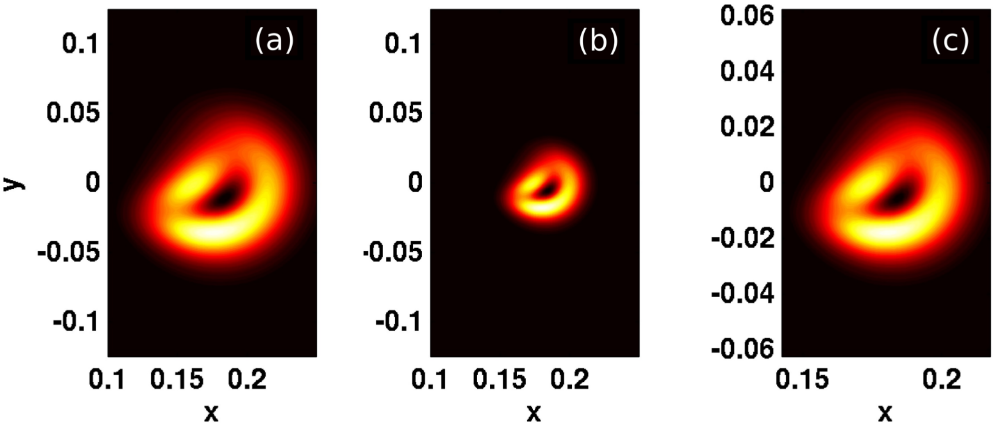

FIG. 7. Comparison of the kinetic energy distributions in the propagating waveform in (a) the baseline (BASE) case and (b), (c) with the value of L_0 halved (BSM). Panel (c) shows panel (b) rescaled by the same factor as L_0 thereby demonstrating that in the magnetically dominated regime the dynamics are essentially unaffected by the vortex length scale. Times shown are $t = 3.01$ for panel (a) and $t = 6.01$ for panels (b) and (c).

The propagating donutlike vortices observed here stand in stark contrast to the solutions predicted by the 1.5-dimensional models used previously. In those solutions, the initial perturbation typically persists in some form over long timescales while emitting slower and smaller propagating waves (e.g., Zeitlin *et al.* [18]), which is essentially a form of dispersive adjustment. The primary waves decay with distance from the initial source. Contrastingly, in the solutions shown above, the initial disturbance splits into two stable, localized waves, which then propagate with constant velocity and with no distortion (except during collisions). It is also interesting to note that whereas we find the magnetic field perturbation to be “locked” with the kinetic energy profile, the 1.5-dimensional solutions of Zeitlin *et al.* [18] have free surface deformations in proportion to the magnetic field perturbation, but no clear relationship between velocity and magnetic field. This is particularly interesting because their model explicitly perturbs the free surface and magnetic field in proportion to one another; our model, however, perturbs only the velocity field and allows the free surface to adjust naturally. Finally, the most obvious difference between our solutions and those from the 1.5-dimensional models is that the donutlike solutions presented here have nontrivial two-dimensional structure that simply cannot be represented in 1.5 dimensions. For instance, the 1.5-dimensional models assume that the horizontal velocity is single-valued as a function of longitudinal position, whereas the flow above and below the center of the donutlike vortex waves run in opposite directions.

B. General parameter space exploration

The simulations discussed in the previous subsection fall in the parameter regime inspired by the radiative layer of the Sun’s tachocline. A notable feature of the solutions is the dominance of magnetic effects in driving the initial vortex to degenerate into zonally propagating Alfvén waves. Since the governing equations apply equally well to other situations, this subsection explores the dynamics in other important regimes. We explored a range of Rossby and Cowling numbers deviating from the BASE case and herein focus on dynamics that exhibit qualitative differences from that of the BASE case.

We begin with the regime of weaker magnetic effects. Figure 8 shows the evolution of the kinetic energy for the case LOW B_{R_0}. A blue grid has been superimposed to clarify changes in size. In contrast to the cases discussed above, no propagating waves are observed on the timescales shown.

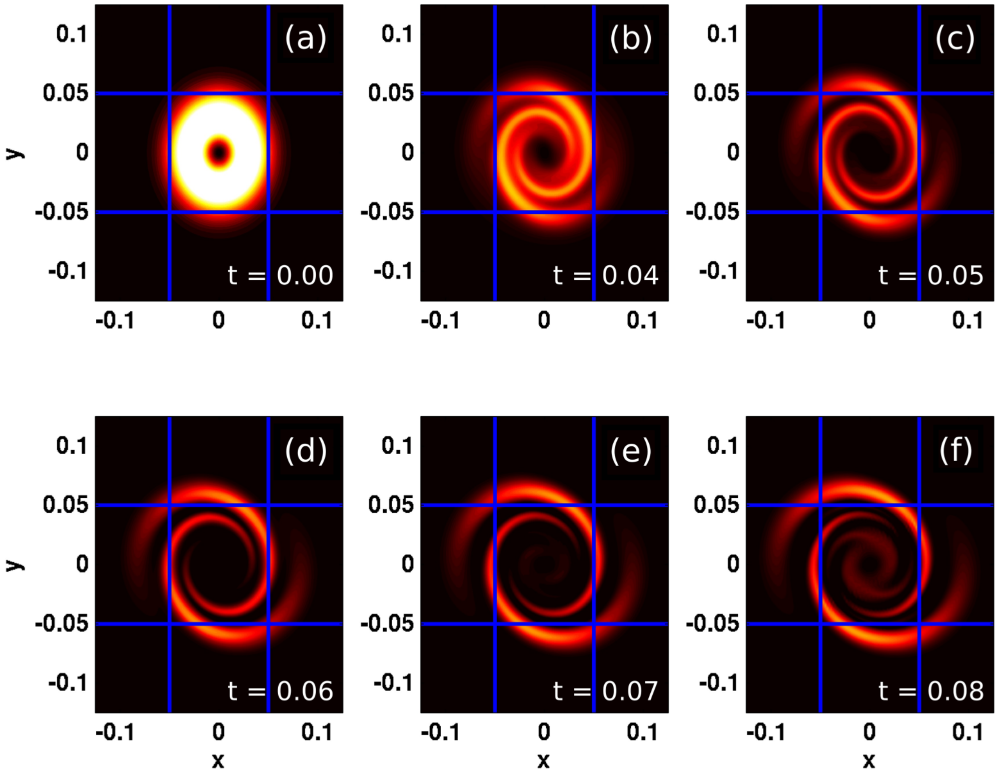

FIG. 8. Plots of the kinetic energy evolution over the course of the simulation when the magnetic field strength is a tenth of that in the baseline case (LOW B_{R_0}). A blue grid is superimposed on the image to show the outward migration of the spiral arms of high KE. Panels (a)–(f) show times $t = 0, 0.04, 0.05, 0.06, 0.07, 0.08$, respectively.

Instead, a spiral is seen to form, sharpen as time goes on, and propagate outward. In particular, notice the manner in which the spiral arm that barely reaches the blue grid in the upper-middle panel [Fig. 8(b)] is well past the grid in the bottom-rightmost panel [Fig. 8(f)]. Also, in the bottom-rightmost panel [Fig. 8(f)] a secondary vortex is seen to form inside the spiral. The weaker magnetic field is unable to enforce the complete locking of the kinetic energy and PMFE fields. This is shown in Fig. 9. Here the kinetic energy field is shaded and three contours of the PMFE field are superimposed in blue. In the outer arms, it can be seen that PMFE contours and high KE regions coincide. The secondary feature in the interior of the spiral that is visible in the bottom-rightmost panel [Fig. 9(f)] does not correspond to a high PMFE region. The lack of locking between the magnetic field and kinetic energy in the secondary vortex led to the creation of sharp gradients and, eventually, wave breaking. This merits future exploration, as part of a more complete study of shocks in SMHD.

To avoid the breaking that was observed in the LOW B_{R_0} case, we systematically reduced the strength of the initial vortex. When the vortex strength is halved, the spiral again forms, as evident in the LOW B_{R_0} LOW U_0 case shown in Fig. 10. The PMFE contours are again superimposed over the shaded KE field. The wind-up of the magnetic field now occurs more slowly, and the Alfvén waves have a chance to separate. By the time shown in the bottom-rightmost panel [Fig. 10(f)], leftward- and rightward-propagating Alfvén waves with a winglike pattern are clearly evident. Note again that the wave shapes in the bottom-middle [Fig. 10(e)] and bottom-right [Fig. 10(f)] panels are essentially identical, even though their shape doesn't resemble the initial condition.

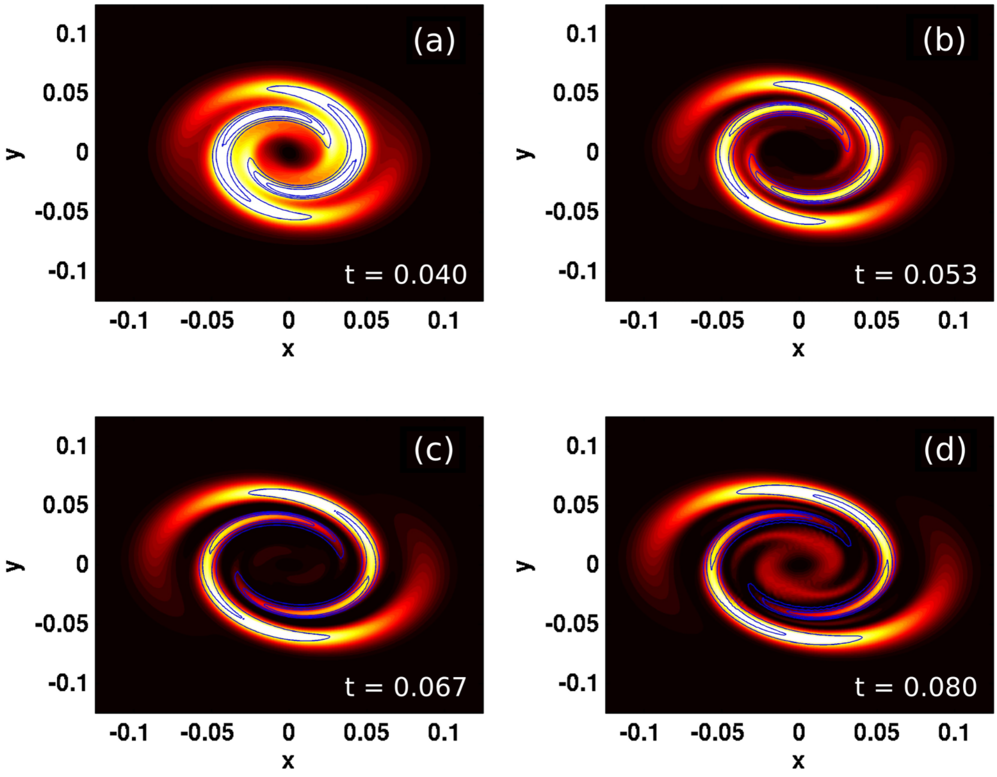

FIG. 9. Shaded contours of the kinetic energy with three contours of PMFE superimposed. The magnetic field strength is a tenth of that in the baseline case (case LOW B_{R_0}). Panels (a)–(d) show times $t = 0.04, 0.053, 0.067, 0.8$, respectively.

Thus even in a parameter regime far from that of the Sun's tachocline, the same Alfvén wave behavior, in which wave shape is "frozen" after adjustment from initial conditions or collisions, is observed.

The above shows that the peculiar nonlinearity of zonally propagating Alfvén waves is observable over a very broad range of parameters. Indeed, it took considerable work to identify a case in which the Alfvén wave dynamics were significantly altered. This was achieved by increasing the rotation rate f while maintaining a fixed magnetic field. We performed a number of exploratory simulations gradually increasing the rotation rate. In Fig. 11 we show the evolution of the kinetic energy for a case with a rotation rate that is 100 times larger than the BASE case (case HIGH f). The ratio of the vortex length scale L to the Rossby radius L_D is 1.8, hence rotation effects are expected to be substantial. Three contours of the PMFE field are superimposed in blue. The Rossby number for this case is 0.037, hence much less than one. Despite this, the general features of the donutlike waves remain largely unchanged. However, in contrast to the BASE case, the donutlike structure no longer propagates in a completely steady manner. Pulsations in the KE and PMFE fields are evident near the front of the wave, below $y = 0$, and at the back of the wave. We have confirmed that the first collision of the waves proceeds in a qualitatively identical manner to the BASE case, in the sense that the waveform is modified during collision but then propagates much as it did prior to the collisions. However, the variability of the waveform is increased, and eventually the nonlinear Alfvén waves are no longer coherent structures confined near $y = 0$. This is demonstrated in Fig. 12, which shows the space-time plot corresponding to Fig. 11. It is evident that while the loss of coherence is not instantaneous, the waveform does degenerate into oscillations after two collisions. In Fig. 13 we

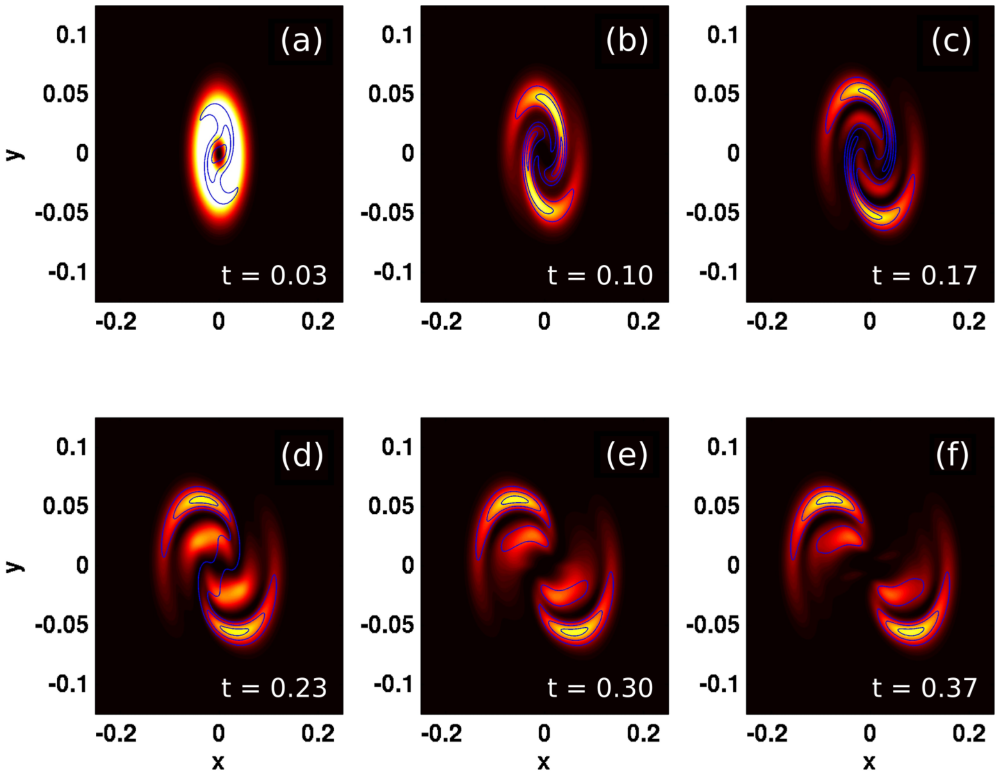

FIG. 10. Plots of the kinetic energy evolution over the course of the simulation when the magnetic field strength is a tenth and U_0 is a half of those in the baseline case (LOW B_{R_0} LOW U_0). Panels (a)–(f) show times $t = 0.03, 0.1, 0.17, 0.23, 0.3, 0.37$, respectively.

show the rightward propagating waveform shape before [Fig. 13(a)], after one [Fig. 13(b)], and after two collisions [Fig. 13(c)]. The waveform does not break down into extremely small-scale structures, but it does change shape with significant nonzero kinetic energy preferentially found away from $y = 0$, the line along which the profiles for the space-time plot are taken. Interestingly, even after two collisions the regions of significant kinetic energy remain locked to regions of PMFE, which are indicated by blue contours.

A 50% reduction in the initial velocity, U_0, did not lead to substantially different dynamics in the HIGH f case, though as expected the asymmetry of the main Alfvén waves was reduced.

IV. DISCUSSION AND CONCLUSIONS

We have studied the evolution of the vortex adjustment problem in SMHD primarily for parameter regimes inspired by the radiative layer of the solar tachocline. In this regime, magnetic effects dominate relative to the other mechanisms (e.g., rotation, buoyancy) in the system. Using our BASE case as a guide, we find that the initial vortex decomposes into two zonally propagating donutlike vortices, which are nonlinear Alfvén waves. The nonlinearity manifests during the initial breakdown of the vortex and leads to more asymmetric wave shapes with increasing vortex strength. These propagate with a fixed form, but are further distorted during head-on collisions. No phase shift is observed during collisions. This suggests that the nonlinear wave dynamics observed in this context are fundamentally different from the soliton paradigm. The behavior observed is generic over a broad range of the parameter space.

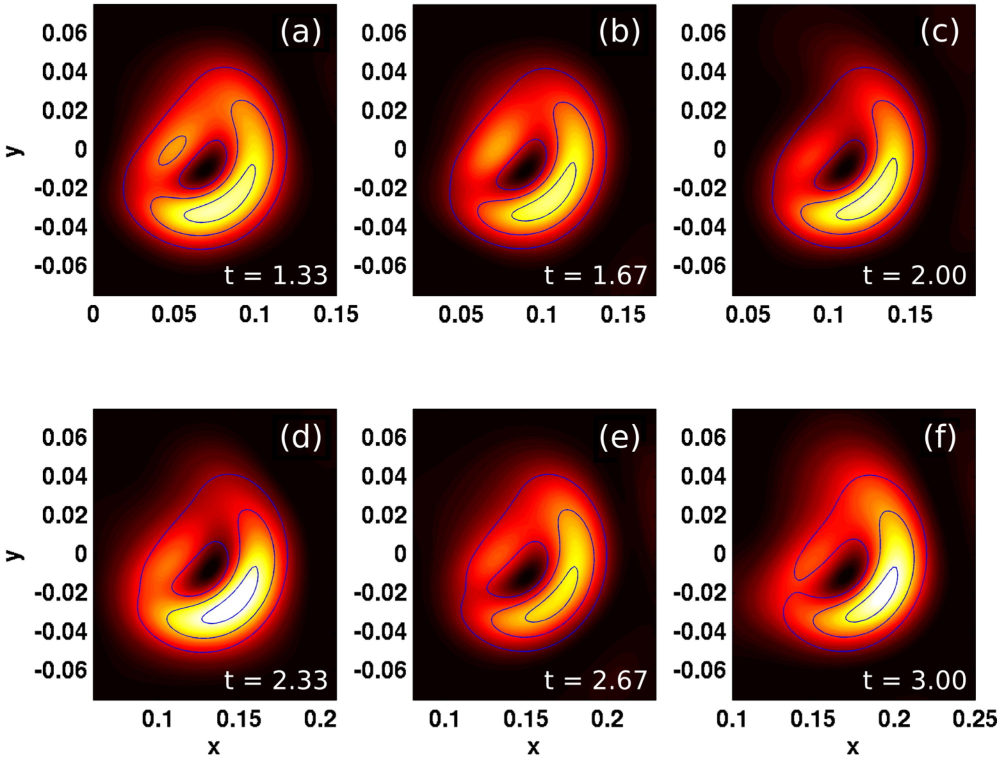

FIG. 11. Evolution of the kinetic energy in the case with f increased 100-fold (HIGH f) at $t = 1.33, 1.67, 2, 2.33, 2.67, 3$ in panels (a)–(f) respectively. Three PMFE contours are superimposed in blue. Note the variability of the waveform shape in this case. Also note that no collisions occur within the time frame shown.

In additional experiments (not shown in the figures), we varied the Atwood number, or buoyancy factor, α over the range appropriate for the radiative layer ($0.01 \leqslant \alpha \leqslant 0.3$). Even at the highest value no discernible difference to the dynamics of the BASE case was observed. The range of α for the overshoot layer is rather different ($10^{-6} \leqslant \alpha \leqslant 10^{-4}$). Here the weak stratification leads to far larger Froude numbers. Nevertheless, experiments with $\alpha = 10^{-6}$ showed again that the initial vortex splits into zonally propagating Alvén waves. The high Froude number manifests as a pinching at the rear of the vortex, eventually leading to sharp, shocklike features. As expected, the free surface deflection is much larger in these cases. Detailed examination of this regime would provide an interesting avenue for future work. Nevertheless, the point again is that Alfvén waves with a nonlinearity of the type described above dominate the dynamics.

The zonally propagating donutlike vortices are coherent structures in the sense discussed by Hughes *et al.* [26]. Specifically, they are stable on timescales much longer than those predicted by simple dimensional arguments. These structures emerge spontaneously from our vortex initial conditions over a wide range of parameters, and, as mentioned previously, we have found that this phenomenon is not very sensitive to the exact functional form used to represent the initial vortex. We therefore expect that any localized perturbation in vorticity in the solar tachocline may decay into these kinds of structures.

The observed behavior in our simulations is consistent with the latitudinal trapping effects suggested by the analysis of London [17]. However, it is unclear whether the method of geometric optics used therein could easily be applied to the study of vortices. The study of 1.5-dimensional models of the tachocline is more common in the literature, though the most recent work, Zeitlin *et al.*

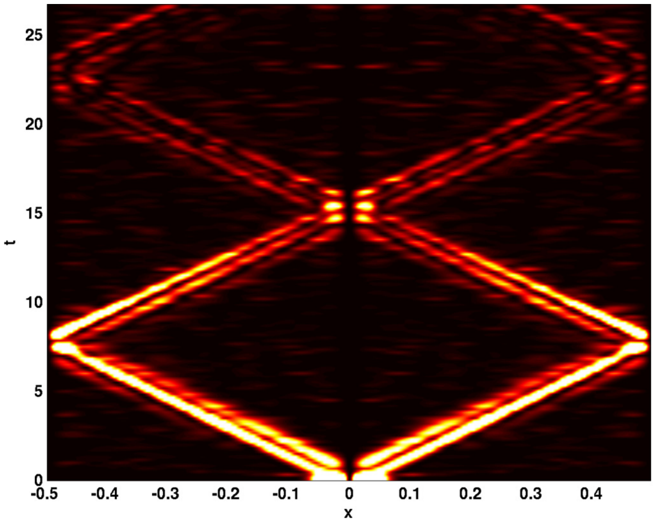

FIG. 12. Space-time plot of the kinetic energy profile along the $y = 0$ transect showing the breakdown of the Alfvén waves for the case with f increased 100-fold (HIGH f).

[18], does not discuss collisions. Indeed, a short calculation based on their parameters suggests that the regime in Zeitlin *et al.* [18] has Co = 1 and Ro < 1, with no Froude number reported. Thus what could be considered the most relevant past study focuses on a fundamentally different region of parameter space than the region explored in this present study. It is worth noting that Zeitlin *et al.* [18] identify wave-wave interactions, or what is termed “weak turbulence,” as an important phenomenon to consider. Our results suggest that for parameter regimes typical of the solar tachocline wave-wave interactions proceed in a very different manner compared to those in pure hydrodynamics, and thus we agree with Zeitlin *et al.* [18], though perhaps for a somewhat different reason.

For weaker magnetic field regimes we demonstrated the possibility of vortex evolution to a spiral state, with a secondary vortex near the center of the spiral. Unlike what was observed for the nonlinear Alfvén waves in the radiative layer of the solar tachocline, and indeed unlike the outer arms of the spiral in this case, the interior region did not exhibit locking between the

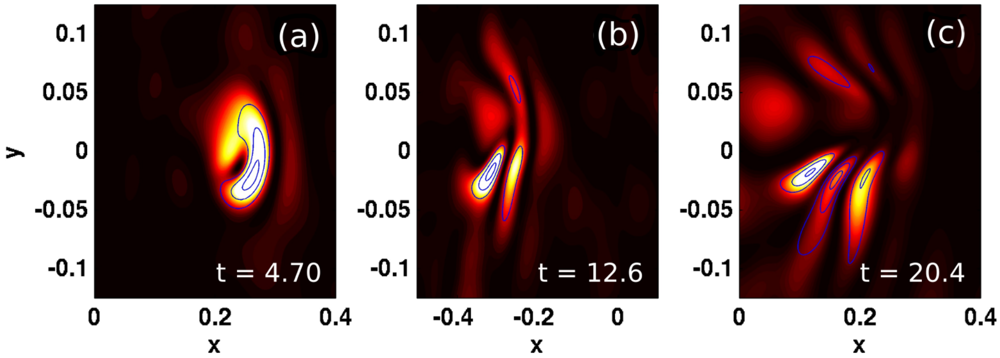

FIG. 13. Evolution of the kinetic energy in the case with f increased 100-fold (HIGH f) (a) before collision, (b) after one collision, and (c) after two collisions. Three PMFE contours are superimposed in blue. Panels (a)–(c) show times $t = 4.7, 12.6, 20.4$, respectively.

kinetic energy and magnetic fields. This led to wave breaking, and the investigation of this regime using shock-resolving models is a clear avenue of future research. When the initial perturbation is weakened, the spiral splits into Alfvén waves, which again remain "frozen" between collisions. However, these Alfvén waves do not have shapes directly related to the initial state.

For extreme states of rotation, we were able to show that the Alfvén waves destabilize, at least partially from the form of the initial vortex. Note that the maximum rotation rate we explored, 100 times the solar rotation rate, is comparable to estimates of the maximum rotations sustainable by real stars. For instance, Stassun *et al.* [39] measured the rotation periods of pre-main-sequence stars in and around the Orion Nebula and reported a minimum rotation period of roughly 0.5 days. By comparison, the rotation period of the Sun is roughly two orders of magnitude slower, at nearly 24 days at the equator and 38 days near the poles. The fastest rotating O-type star observed appears to be VFTS102, which has a projected rotation velocity of over 500 km s^{-1}, at least two orders of magnitude faster than the Sun [40,41]. Of course, as stellar rotation rates approach these limiting values, the overall structure of the stars are also considerably deformed. Hence our HIGH f experiment is an extreme upper bound on the rotation rates that could be sustained in reality. Even under such extreme conditions, however, the Alfvén wave destabilization only occurs gradually. The general observations based on the tachocline case still hold for a lengthy period of time.

ACKNOWLEDGMENTS

This work was supported by the Natural Sciences and Engineering Research Council of Canada (NSERC) through Discovery Grant RGPIN-311844-37157. In addition, A.C. received financial support from the NSERC CGS D scholarship, B.A.S. from the Queen Elizabeth II scholarship, and M.M. from the Ontario Graduate scholarship.

[1] G. K. Vallis, *Atmospheric and Oceanic Fluid Dynamics* (Cambridge University Press, Cambridge, 2017).

[2] P. Brandt, A. Rubino, W. Alpers, and J. O. Backhaus, Internal waves in the Strait of Messina studied by a numerical model and synthetic aperture radar images from the *ERS* 1/2 satellites, J. Phys. Oceanogr. **27**, 648 (1997).

[3] A. de la Fuente, K. Shimizu, J. Imberger, and Y. Niño, The evolution of internal waves in a rotating, stratified, circular basin and the influence of weakly nonlinear and nonhydrostatic accelerations, Limnol. Oceanogr. **53**, 2738 (2008).

[4] G. Whitham, *Linear and Nonlinear Waves*, Pure and Applied Mathematics: A Wiley Series of Texts, Monographs and Tracts, Vol. 42 (Wiley-Interscience, New York, 1999).

[5] A. C. Kuo and L. M. Polvani, Nonlinear geostrophic adjustment, cyclone/anticyclone asymmetry, and potential vorticity rearrangement, Phys. Fluids **12**, 1087 (2000).

[6] R. Grimshaw, C. Guo, K. Helfrich, and V. Vlasenko, Combined effect of rotation and topography on shoaling oceanic internal solitary waves, J. Phys. Oceanogr. **44**, 1116 (2014).

[7] A. Coutino and M. Stastna, The fully nonlinear stratified geostrophic adjustment problem, Nonlin. Process. Geophys. **24**, 61 (2017).

[8] P. A. Gilman, Magnetohydrodynamic "shallow water" equations for the solar tachocline, Astrophys. J. **544**, L79 (2000).

[9] D. A. Schecter, J. F. Boyd, and P. A. Gilman, "shallow-water" magnetohydrodynamic waves in the solar tachocline, Astrophys. J. **551**, L185 (2001).

[10] H. De Sterck, Hyperbolic theory of the "shallow water" magnetohydrodynamics equations, Phys. Plasmas **8**, 3293 (2001).

[11] P. J. Dellar, Dispersive shallow water magnetohydrodynamics, Phys. Plasmas **10**, 581 (2003).

[12] F. Gu, Y. Lu, and Q. Zhang, Global solutions to one-dimensional shallow water magnetohydrodynamic equations, J. Math. Anal. Appl. **401**, 714 (2013).

[13] M.-C. Shiue, An initial boundary value problem for one-dimensional shallow water magnetohydrodynamics in the solar tachocline, Nonlinear Anal. **76**, 215 (2013).
[14] V. Zeitlin, Remarks on rotating shallow-water magnetohydrodynamics, Nonlin. Process. Geophys. **20**, 893 (2013).
[15] T. Zaqarashvili, R. Oliver, J. Ballester, and B. Shergelashvili, Rossby waves in "shallow water" magnetohydrodynamics, Astron. Astrophys. **470**, 815 (2007).
[16] T. Zaqarashvili, R. Oliver, and J. Ballester, Global shallow water magnetohydrodynamic waves in the solar tachocline, Astrophys. J. Lett. **691**, L41 (2009).
[17] S. D. London, Weakly nonlinear shallow water magnetohydrodynamic waves, Geophys. Astrophys. Fluid Dyn. **108**, 323 (2014).
[18] V. Zeitlin, C. Lusso, and F. Bouchut, Geostrophic vs magneto-geostrophic adjustment and nonlinear magneto-inertia-gravity waves in rotating shallow water magnetohydrodynamics, Geophys. Astrophys. Fluid Dyn. **109**, 497 (2015).
[19] F. J. Poulin, A. Borissov, B. A. Storer, and M. Stastna, A shallow water model of the solar tachocline: A numerical approach to determine wave structure, Dyn. Contin. Discrete Impuls. Syst. Ser. B Appl. Alg. **25**, 219 (2018).
[20] T. V. Zaqarashvili, R. Oliver, A. Hanslmeier, M. Carbonell, J. L. Ballester, T. Gachechiladze, and I. G. Usokin, Long-Term variation in the sun's activity caused by magnetic rossby waves in the tachocline, Astrophys. J. Lett. **805**, L14 (2015).
[21] X. Márquez-Artavia, C. Jones, and S. Tobias, Rotating magnetic shallow water waves and instabilities in a sphere, Geophys. Astrophys. Fluid Dyn. **111**, 282 (2017).
[22] T. Kröger and M. Lukáčová-Medvid'ová, An evolution Galerkin scheme for the shallow water magnetohydrodynamic equations in two space dimensions, J. Comput. Phys. **206**, 122 (2005).
[23] S. Qamar and G. Warnecke, Application of space-time CE/SE method to shallow water magnetohydrodynamic equations, J. Comput. Appl. Math. **196**, 132 (2006).
[24] S. Qamar and S. Mudasser, A kinetic flux-vector splitting method for the shallow water magnetohydrodynamics, Comput. Phys. Commun. **181**, 1109 (2010).
[25] S. Zia, M. Ahmed, and S. Qamar, Numerical solution of shallow water magnetohydrodynamic equations with non-flat bottom topography, Int. J. Comput. Fluid Dyn. **28**, 56 (2014).
[26] D. W. Hughes, R. Rosner, and N. O. Weiss, *The Solar Tachocline* (Cambridge University Press, Cambridge, 2007).
[27] M. Dikpati, P. S. Cally, S. W. McIntosh, and E. Heifetz, The origin of the "seasons" in space weather, Sci. Rep. **7**, 14750 (2017).
[28] E. Spiegel and J.-P. Zahn, The solar tachocline, Astron. Astrophys. **265**, 106 (1992).
[29] T. S. Wood and N. H. Brummell, A self-consistent model of the solar tachocline, Astrophys. J. **853**, 97 (2018).
[30] E. J. Hopfinger and G. J. F. van Heijst, Vortices in rotating fluids, Annu. Rev. Fluid Mech. **25**, 241 (1993).
[31] J. N. Bahcall and M. H. Pinsonneault, What do we (not) Know Theoretically About Solar Neutrino Fluxes? Phys. Rev. Lett. **92**, 121301 (2004).
[32] H. B. Snodgrass and R. K. Ulrich, Rotation of Doppler features in the solar photosphere, Astrophys. J. **351**, 309 (1990).
[33] B. S. Ryden, B. M. Peterson, and M. Demianski, *Foundations of Astrophysics* (Addison-Wesley, New York, 2010).
[34] J. Mak, S. D. Griffiths, and D. W. Hughes, Shear flow instabilities in shallow-water magnetohydrodynamics, J. Fluid Mech. **788**, 767 (2016).
[35] D. J. Acheson, *Elementary Fluid Dynamics* (Oxford University Press, Oxford, 1990).
[36] D. T. Steinmoeller, M. Stastna, and K. G. Lamb, Fourier pseudospectral methods for 2D Boussinesq-type equations, Ocean Model. **52–53**, 76 (2012).
[37] C. J. Subich, K. G. Lamb, and M. Stastna, Simulation of the Navier-Stokes equations in three dimensions with a spectral collocation method, Int. J. Numer. Methods Fluids **73**, 103 (2013).
[38] J. Christensen-Dalsgaard, The 'standard' sun modelling and helioseismology, Space Sci. Rev. **85**, 19 (1998).

[39] K. G. Stassun, R. D. Mathieu, T. Mazeh, and F. J. Vrba, The rotation period distribution of pre-main-sequence stars in and around the orion nebula, Astron. J. **117**, 2941 (1999).

[40] P. L. Dufton, P. R. Dunstall, C. J. Evans, I. Brott, M. Cantiello, A. de Koter, S. E. de Mink, M. Fraser, V. Hénault-Brunet, I. D. Howarth *et al.*, The VLT-FLAMES Tarantula Survey: The fastest rotating O-type star and shortest period LMC pulsar-remnants of a supernova disrupted binary? Astrophys. J. Lett. **743**, L22 (2011).

[41] D. Jiang, Z. Han, L. Yang, and L. Li, The binary merger channel for the progenitor of the fastest rotating O-type star VFTS 102, Mon. Not. R. Astron. Soc. **428**, 1218 (2012).